


FULL PAPER

Open Access



A statistical study of convective and dynamic instabilities in the polar upper mesosphere above Tromsø

Satonori Nozawa^{1*} , Norihito Saito², Takuya Kawahara³, Satoshi Wada², Takuo T. Tsuda⁴, Sakiho Maeda¹, Toru Takahashi⁵, Hitoshi Fujiwara⁶, Viswanathan Lakshmi Narayanan⁷, Tetsuya Kawabata¹ and Magnar G. Johnsen⁸

Abstract

We have studied the convective (or static) and dynamic instabilities between 80 and 100 km above Tromsø (69.6° N, 19.2° E) using temperature and wind data of 6 min and 1 km resolutions primarily almost over a solar cycle obtained with the sodium lidar at Tromsø. First, we have calculated Brunt–Väisälä frequency (N) for 339 nights obtained from October 2010 to December 2019, and the Richardson number (Ri) for 210 nights obtained between October 2012 to December 2019. Second, using those values (N and Ri), we have calculated probabilities of the convective instability ($N^2 < 0$) and the dynamic instability ($0 \leq Ri < 0.25$) that can be used for proxies for evaluating the atmospheric stability. The probability of the convective instability varies from about 1% to 24% with a mean value of 9%, and that of the dynamic instability varies from 4 to 20% with a mean value of 10%. Third, we have compared these probabilities with the F10.7 index and local K -index. The probability of the convective instability shows a dependence (its correlation coefficient of 0.45) of the geomagnetic activity (local K -index) between 94 and 100 km, suggesting an auroral influence on the atmospheric stability. The probability of the dynamic instability shows a solar cycle dependence (its correlation coefficient being 0.54). The probability of the dynamic instability shows the dependence of the 12 h wave amplitude (meridional and zonal wind components) ($C.C. = 0.52$). The averaged potential energy of gravity waves shows decrease with height between 81 and 89 km, suggesting that dissipation of gravity waves plays an important role (at least partly) in causing the convective instability below 89 km. The probability of the convective instability at Tromsø appears to be higher than that at middle/low latitudes, while the probability of the dynamic instability is similar to that at middle/low latitudes.

Keywords Polar upper mesosphere, Sodium lidar, Convective instability, Dynamic instability, Static instability, Semidiurnal tide, Gravity wave dissipation, Brunt–Väisälä frequency, Richardson number

*Correspondence:

Satonori Nozawa

nozawa@isee.nagoya-u.ac.jp

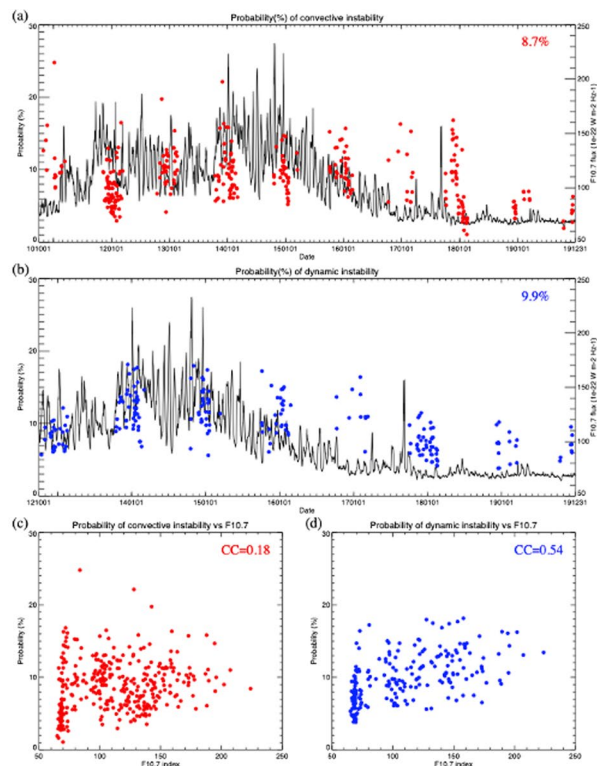
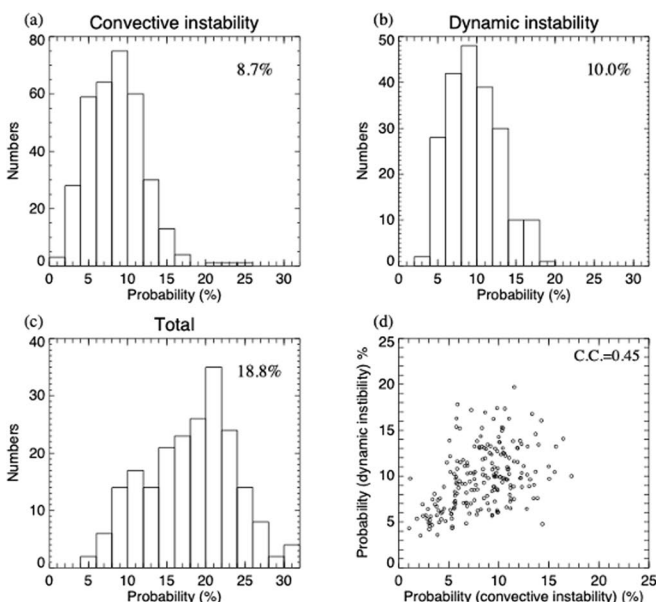
Full list of author information is available at the end of the article



© The Author(s) 2023. **Open Access** This article is licensed under a Creative Commons Attribution 4.0 International License, which permits use, sharing, adaptation, distribution and reproduction in any medium or format, as long as you give appropriate credit to the original author(s) and the source, provide a link to the Creative Commons licence, and indicate if changes were made. The images or other third party material in this article are included in the article's Creative Commons licence, unless indicated otherwise in a credit line to the material. If material is not included in the article's Creative Commons licence and your intended use is not permitted by statutory regulation or exceeds the permitted use, you will need to obtain permission directly from the copyright holder. To view a copy of this licence, visit <http://creativecommons.org/licenses/by/4.0/>.

Graphical Abstract

Probabilities of the convective and dynamic instabilities above Tromsø (69.6°N, 19.2°E)



Introduction

The polar mesosphere and lower thermosphere (MLT) is one of the unique regions in terms of the vertical coupling between the magnetosphere and atmosphere. The solar wind energy comes into the lower thermosphere, and even the mesosphere, but its quantitative effect on the MLT is still poorly understood. Atmospheric waves (gravity, tidal, and planetary waves) are generated in the troposphere and stratosphere, and propagate upward with their amplitudes growing. Most gravity waves break in the upper mesosphere (in particular, around the mesopause region), and provide energy and momentum to the atmosphere there, and generate atmospheric instabilities (e.g., Fritts and Alexander 2003). This paper investigates probabilities of the convective and dynamic instabilities (e.g., Stull 2020) of the atmosphere in the polar upper mesosphere and their causes. The atmosphere becomes unstable when the vertical temperature gradient becomes less than $-g/C_p$ ($= -9.5$ K/km at around 100 km in altitude; C_p is the constant pressure specific heat and g is the gravitational acceleration: 9.5 m/s² in the mesopause region); this is the convective (or static) instability occurring mainly in the troposphere. In the upper mesosphere,

it is convectively stable on average, but some disturbances (e.g., gravity waves and tidal waves) make the atmosphere unstable from time to time (e.g., Zhao et al. 2003). Zhao et al. (2003) using 32 night/195 h data obtained at Albuquerque, NM (35° N, 106.5° W) showed that the semidiurnal tide has significant impacts on the distribution of the convectively unstable region. Li et al. (2005) using 19 night/133 h data obtained at Maui, Hawaii (20.7° N, 156.3° W) identified links between instabilities and mesospheric inversion layers, and consistent correlation of the atmospheric convective stabilities with the vertical shear in horizontal winds. Li et al. (2005) pointed out that the instability is almost always present at some altitudes (between 85 and 100 km) at a given time. Sherman and She (2006) using data obtained at Fort Collins, CO (41° N, 105° W) focused on altitude-resolved statistics. Maximum wind shears were most often observed at 100 km in winter, while maximum shears were least likely observed near the sodium layer centroid (90–93 km) in winter when the observed wind shears were larger than those observed in other seasons. Large shears were observed most often in winter, possibly due to increased gravity wave activity near winter solstice. To evaluate

the convective stability, temperature measurements are required as a function of altitude; metal resonance lidars can provide temperature data with good quality as a function of altitude and time. Furthermore, some sodium lidars can provide wind velocity data as well. Brunt–Väisälä frequency (Emanuel 1994) and Richardson number (Kundu et al. 1990) can be calculated as follows:

$$N = \sqrt{\frac{g}{T} \left(\frac{\partial T}{\partial z} + \frac{g}{C_p} \right)}, \quad (1)$$

$$\text{Ri} = \frac{N^2}{\left(\frac{du}{dz} \right)^2 + \left(\frac{dv}{dz} \right)^2}, \quad (2)$$

where T is temperature, z is altitude, u and v are zonal and meridional wind velocities. When N^2 becomes negative, the atmosphere is convectively unstable, and when Ri becomes smaller than $1/4$, the atmosphere can be dynamically unstable. The convective instability is characterized by the vertical gradient of the temperature, while the dynamic instability is determined by both the vertical temperature gradient as well as the vertical shear of the horizontal winds. Li et al. (2005) pointed out that the dynamical instability, in a statistical sense, is a result of the combination of reduced convective stability and enhanced wind shear.

As far as we know, there are four statical studies published which investigated the convective and dynamic stabilities in the upper mesosphere: they were conducted at Starfire optical range, New Mexico (35.0° N, 106.5° W) (Zhao et al. 2003), Maui, Hawaii (20.7° N, 156.3° W) (Li et al. 2005), Fort Collins, Colorado (41.1° N, 105.1° W) (Sherman and She 2006), and São José dos Campos (23.1° S, 45.9° W) (Andrioli et al. 2017). The data of all the studies were obtained at middle/low latitudes. We conducted the first statistical study about the atmospheric stabilities in the polar upper mesosphere (80–100 km) at high latitudes, where the solar wind energy input is present from time to time, from October to March in the Northern hemisphere. The primary purpose of this paper is to present observational results of the convective and dynamic instability occurrence between 80 and 100 km in the polar (winter) upper mesosphere. First, we will show sample data of temperature and wind obtained on the night of December 19, 2018, and then show variations of the square of Brunt–Väisälä frequency and Richardson number as functions of time and altitude. Next, we introduce probabilities of the instabilities. Then, statistical results will be presented. We will show correlations between the probabilities and several parameters (F10.7 index, local K -index, 12 h wave amplitude). Finally, based on these results with an altitude profile of the potential

energy of gravity waves (GWs), we will suggest the causes of the convective and dynamic instabilities in the polar upper mesosphere. In this study, only vertical changes of temperature and wind were analyzed. Possible other instabilities from inertia and rotation, horizontal wind shear (cf. Sedlak et al. 2021) or non-local turbulence could not be evaluated.

Datasets

The sodium lidar at Tromsø started observations of temperature and sodium density in October 2010 (see Nozawa et al. 2014). Details of the sodium lidar system were described in Nozawa et al. (2014) as well as Kawahara et al. (2017). Since October 2012, we have operated the sodium lidar with a five-beam mode in which the laser is emitted simultaneously in five directions (vertical, south, north, west, and east), and scatter light from the sodium layer is received using five receiving systems. This mode allows us to derive vertical, northward, and eastward winds velocities. In this study, we used data whose data cover at 90 km is longer than 4 h per night. The maximum error values accepted are set to be 5 K and 15 m/s to derive probabilities.

In total, we have temperature and wind data for 339 nights (3724 h) and 210 nights (2048 h), respectively. Figure 1a, b, c, d shows in histograms how many days and hours per month could be used for the convective instability analysis (a and b) and the dynamic one (c and d), respectively.

Both the number of days and hours are the largest in December and January, and the smallest in October and March. The number of the data obtained between October 20 and February 20 (i.e., in winter) is 298 days (3408 h) and 185 days (1874 h) for temperature and wind data, respectively. It should be kept in mind that almost all the data (~90%) were obtained in winter. This is mainly because of no dark periods during summer and longer twilight hours during equinoxes. We used the Lomb–Scargle method for deriving 12 h, 8 h, and 6 h periodic (wave) components, which is based on least-squares frequency analysis of unequally spaced data (cf. Hocke 1998, and reference therein). To derive 12 h and 6 h wave components, we used only those nights with a measurement duration longer than 12 h with data availability of at least 55% of the value of those measurements. In total, we collected 248 nights and 154 nights of temperature and wind datasets for derivations of the 12 h and 6 h components, respectively. We used 16-h length data (data coverage being larger than 55%) to derive an 8-h component. These 3 periodic components (with a mean value) were used to calculate the background temperature when we derived the potential energy of gravity waves (Eq. 5). The 12-h component is treated as the

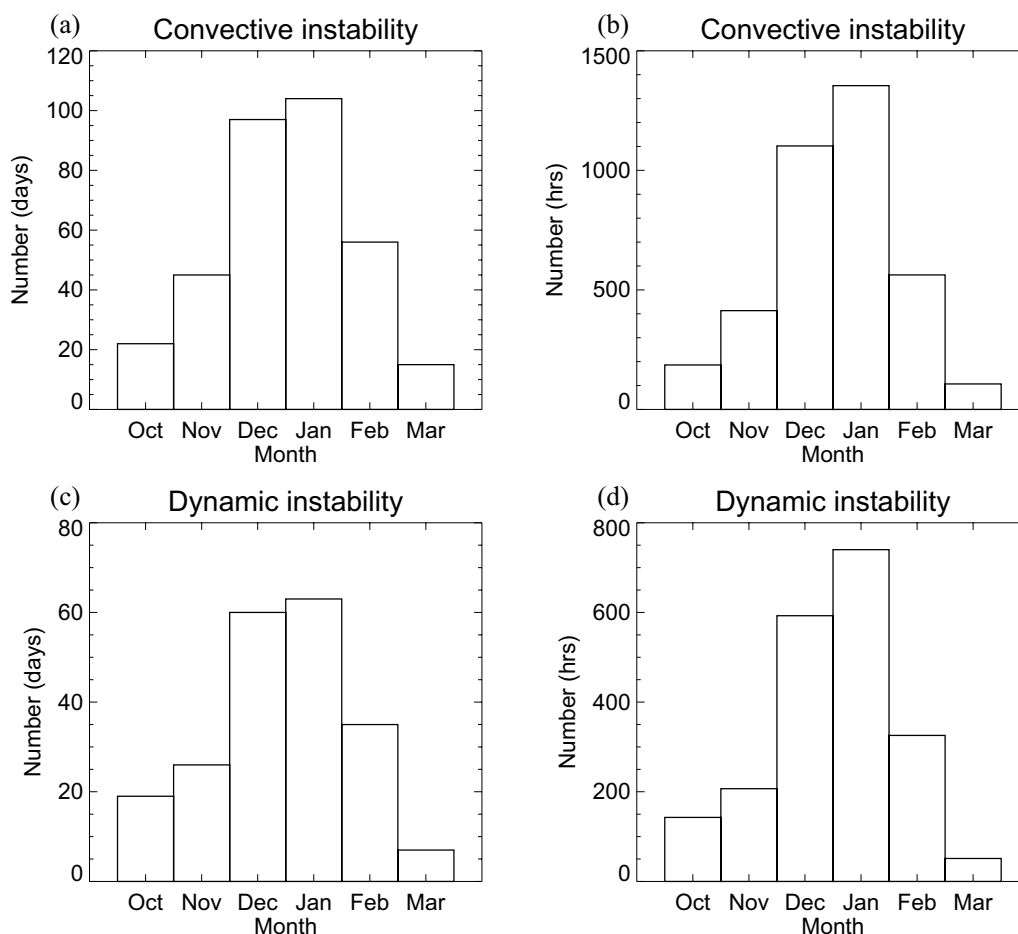


Fig. 1 Histograms of the number of days and hours. Histograms of the number of days used for the **a** convective and **c** dynamic instabilities, and the number of hours used for the **b** convective and **d** dynamic instabilities

semidiurnal tide in this study. It should be kept in mind that we had to ignore a possible contribution of the 24-h component. The 24-h amplitude is believed to be smaller than that of the 12-h amplitude in the polar upper mesosphere (Pancheva et al. 2020), but it would play a role (at least partly). However, due to the usage of nightly observational data (19 h at longest), we cannot derive the 24-h component properly. This is one of limitations of this study.

To investigate the possible relation between the atmospheric instabilities and auroral effects, we used the local *K*-index at Tromsø. The *K*-index is a frequently used geomagnetic activity index which goes far back in time (e.g., Bartels et al. 1939). The index is derived from magnetic observatory data, more specifically, the two horizontal components. The goal is to have the index represent geomagnetic variations of external, solar-terrestrial interaction, origin, and therefore the Earth internal and crustal magnetic field component as well as the Solar Quiet (*Sq*) variation is

removed. Then the largest range among the two horizontal components (north and east) is taken, and a number between 0 and 9 is assigned according to a predefined scale. The scale is based on the Niemegk Observatory scale and adjusted according to local conditions and latitude. Owing to pragmatic reasons and history, the Tromsø *K*-index calculation is based on an empirical *Sq* variation model, and only the H-component is considered. This is easily justified by Tromsø being in the auroral zone, where disturbances are generally of a much larger magnitude (100 s of nT) compared to the *Sq* variation (~70 nT during summer) as opposed to observatories further south. Furthermore, the H-component is the dominant component associated with the magnetic disturbances seen, owing to the east–west nature of auroral currents. Because of the simplification described above, it may be assumed that the Tromsø *K*-values have an uncertainty of about 1 for the lower activities, but the difference is insignificant for higher activities. In Tromsø, *K*=9 corresponds to a range of

2000 nT or above. When referring to the local *K*-index or just *K*-index in this manuscript, we are referring to the *K*-index for Tromsø magnetic observatory (TRO).

Results

We first present variations of temperature, its error values, and horizontal winds, and then the Brunt–Väisälä frequency and Richardson number obtained on the night of December 19, 2018.

A case on December 19, 2018

Figure 2a shows temporal variations of the neutral temperature between 75 and 110 km with 6 min time and 1 km height resolutions from 12 UT on December 19 to 09 UT on December 20, 2018 in the vertical direction (out of the 5 directions) obtained by the sodium lidar at Tromsø. Only data with error values less than 5 K are presented. In this study, we mainly present data with 6 min/1 km resolutions. If the weather permitted, we were able to obtain temperature data for ~19 h per night during months around winter solstice (i.e., December and January). The neutral temperature generally decreases with increasing height, and wavy structures, where the higher (or lower) temperature region decreases

with time, can be clearly found above 90 km, probably due to the semidiurnal tide (or a 12 h gravity wave). Below 90 km, temporal/altitude variations probably due to shorter periodic waves (i.e., gravity waves) can be seen. The mean temperature over the time and height region on this night is ~199 K. Figure 2b shows corresponding error values. The error values sharply increase around the bottom edge of the sodium layer (say below 80 km) as the height decreases. In the figure, two black solid lines with error values of 2 K (~1% of the mean temperature) and 5 K (~2.5% of the mean value) are presented. Since the sodium density is higher between about 85 and 97 km, error values are below 2 K.

Starting on October 6, 2012, we have made simultaneous five-directional measurements (vertical, south, north, west, east) with the 3-frequency mode (She and Yu 1994), allowing us to derive wind velocities together with neutral temperature and sodium density. Two observational configurations were conducted: one used an elevation angle of 60° for 4 years in the 2012, 2017, 2018, and 2019 seasons, while another pattern used an elevation of 77.5° for 4 years in the 2013, 2014, 2015, and 2016 seasons. Since our lidar measurements are conducted from October to March, we refer to as a season of observations.

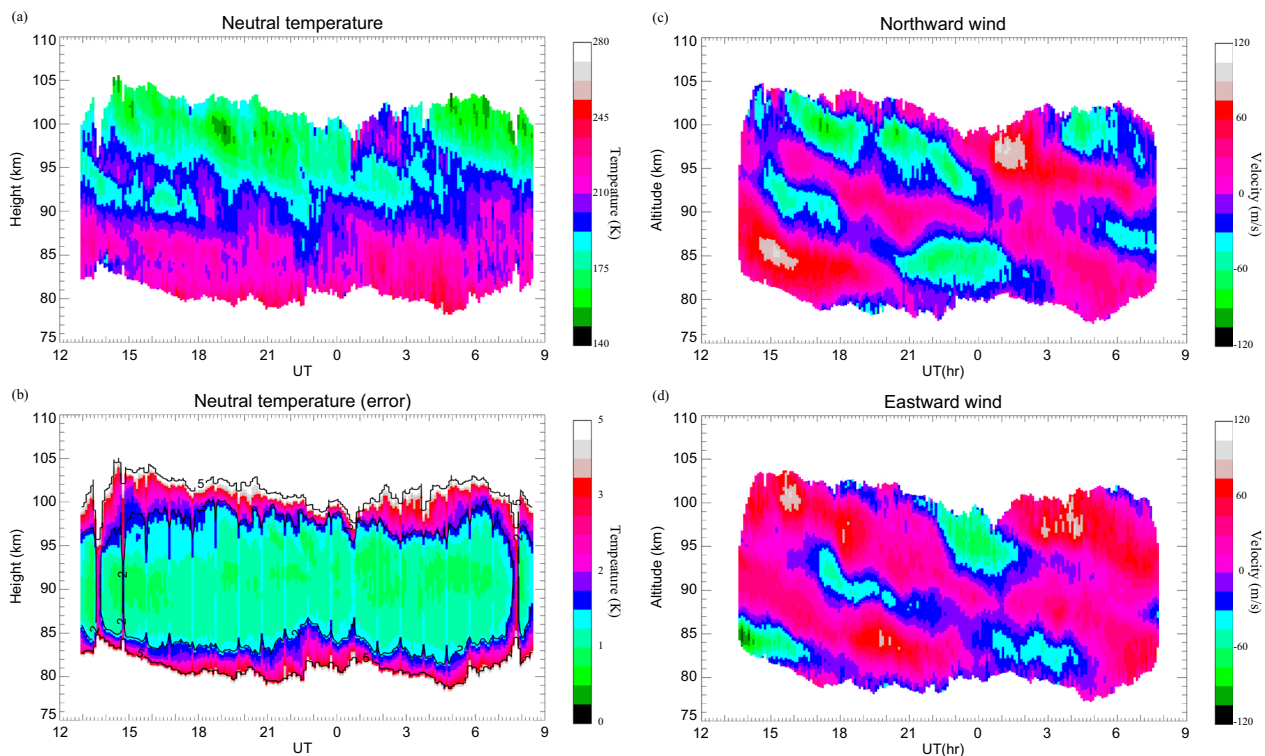


Fig. 2 Variations of temperature, error values, northward and eastward wind on December 19, 2018. Temporal and altitude variations of **a** temperature, **b** its error values, **c** northward and **d** eastward winds obtained with the sodium lidar at Tromsø on December 19, 2018

For example, the 2012 season corresponds to the time interval from October 2012 to March 2013. To assure the beam directions, we used star images similar to those we made for the photometer positioning (see Nozawa et al. 2018). Figure 2c, d shows temporal variations of northward and eastward wind velocities, respectively, over ~ 16 h from 13 UT on December 19 and 06 UT on December 20, 2018 as a function of height from 75 and 110 km. Data with error values less than 15 m/s are presented. The positive (negative) values correspond to the northward (southward) and the eastward (westward) directions. The reason why the wind measurement intervals are shorter than that of the temperature measurements is that we sometimes make 1-beam (only toward the vertical position) measurements for ~ 40 – 50 min during the twilight period surrounding the night (darkness) hours. In the vertical mode, we transmit all the laser power (about ~ 3.5 W) toward the vertical direction, so a signal five times stronger than that of the five-direction mode (~ 0.7 W each) can be obtained, allowing us to make reasonable observations under higher background noise conditions (solar illumination scatter). In Fig. 2c, d, wavy structures can be seen over the height region. For example, in Fig. 2d, an eastward wind region with a strength of ~ 60 m/s is seen at around 91 km at 14 UT, and decreases as time goes on, and reaches ~ 83 km at 21 UT. Also, it can be observed that vertical shears in the horizontal winds occur through the night. It should be pointed out that the wavy structures can be seen more clearly in wind data than in temperature data.

Figure 3a shows variations of square of Brunt–Väisälä frequency (N^2) derived on December 19, 2018. Negative N^2 values are denoted by black rectangles. Again, wavy structures probably due to tides and GWs are found. The averaged value of N^2 is 0.00034 rad/s (corresponding Brunt–Väisälä period being 341 s) over the night, and averaged error value is 0.000132 rad/s. The atmosphere is convectively stable most of the time, and the probability of the convective instability is $\sim 5.0\%$ on this night. Figure 3b shows variations of the Richardson number (Ri) on the same night. It varied from some negative values to ~ 4 . Negative Ri (i.e., negative N^2) regions are denoted by black rectangles. To show dynamic unstable regions ($0 \leq \text{Ri} < 1/4$) more clearly, in Fig. 3c, such unstable regions are denoted by red rectangles, while negative Ri regions are shown by black rectangles as well, and stable regions are denoted by green rectangles. On the night, the probability of dynamic instability is $\sim 10.2\%$, thus $\sim 15\%$ (in total) of time and height regions became unstable. It should be kept in mind that unfortunately error values of Ri are relatively large, since the wind velocity measurements are involved some error values (e.g., the averaged error values are about 4 m/s for the night of December 19, 2018).

Distribution of probabilities

We calculated the probabilities of the convective and dynamic instabilities for 339 nights and 210 nights, respectively. The probabilities of the convective ($P(N^2 < 0)$) and dynamic ($P(0 \leq \text{Ri} < 0.25)$) instabilities are calculated as follows (Zhao et al. 2003):

$$P(N^2 < 0) = \frac{\text{Number of data with } N^2 < 0}{\text{Number of data}} \times 100(\%), \quad (3)$$

$$P(0 \leq \text{Ri} < 0.25) = \frac{\text{Number of data with } 0 < \text{Ri} < 0.25}{\text{Number of data}} \times 100(\%). \quad (4)$$

Figure 4a, b, c shows histograms of the probabilities of the convective instability, the dynamic instability, and the sum of both (i.e., $\text{Ri} < 1/4$) between 80 and 100 km, respectively. Note that Fig. 4c contains data from 210 days in which both N^2 and Ri values are available. Mean values are 8.7% [standard deviation (SD)=3.6%], 10.0% (SD=3.5%), and 18.8% (SD=5.9%) for the probabilities of the convective and dynamic instabilities, and the sum of them, respectively. The shapes of the distribution of the probabilities of the convective and dynamic instabilities are fairly symmetric around the mean values. Comparing Fig. 4a, b, it can be seen that the dynamic instability occurs slightly more often than the convective instability. The probability of the convective instability varies from about 1% to 24%, and that of the dynamic instability varies from 4 to 20%. The distribution of the total probabilities is broader than those of the probabilities of the convective and dynamic instabilities, and ranges from 5 to 31%. Figure 4d shows a scatter plot between the probabilities of the convective and dynamic instabilities. Its correlation coefficient is ~ 0.45 , indicating a bit weak correlation between them. This implies the contribution of wind shears which also plays an important role in the dynamic instability in addition to the vertical temperature gradient, and the tidal and gravity waves play important roles in making such a shear of the horizontal winds. When we use data with 15 min and 30 min temporal and 1 km altitude resolutions, the correlation shows no significant changes (correlation coefficient = ~ 0.50 and ~ 0.42 , respectively).

Altitude profiles of the probabilities

Figure 5 compares the altitude profiles of the probabilities of the convective (black) and dynamic (red) instabilities, and their sum (blue) from 80 to 100 km with a 1-km step. The probabilities at each height are calculated using all the data at the same height (not averaging probabilities on nights). The probability of the convective instability shows a minimum value ($\sim 4\%$) at 91 km; it increases downwards from 91 to

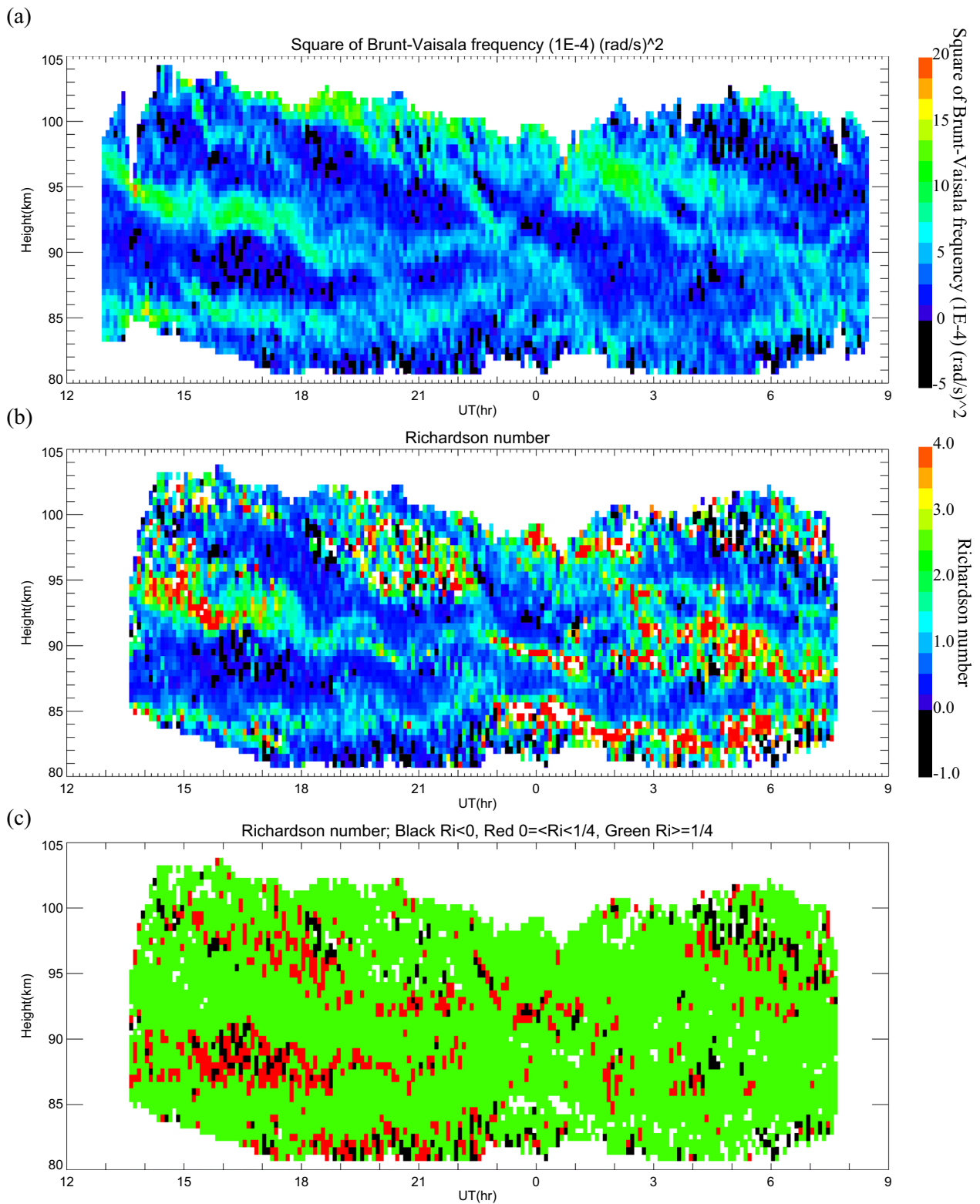


Fig. 3 Variations of square of Brunt–Väisälä frequency, and Richardson number. Variations of **a** square of Brunt–Väisälä frequency, **b** Richardson number, and **c** modified Richardson number. Data with $N^2 < 0$ are denoted by black rectangles. In **c**, data with $0 \leq Ri < 1/4$ are denoted by red rectangles, and stable regions are denoted by green rectangles

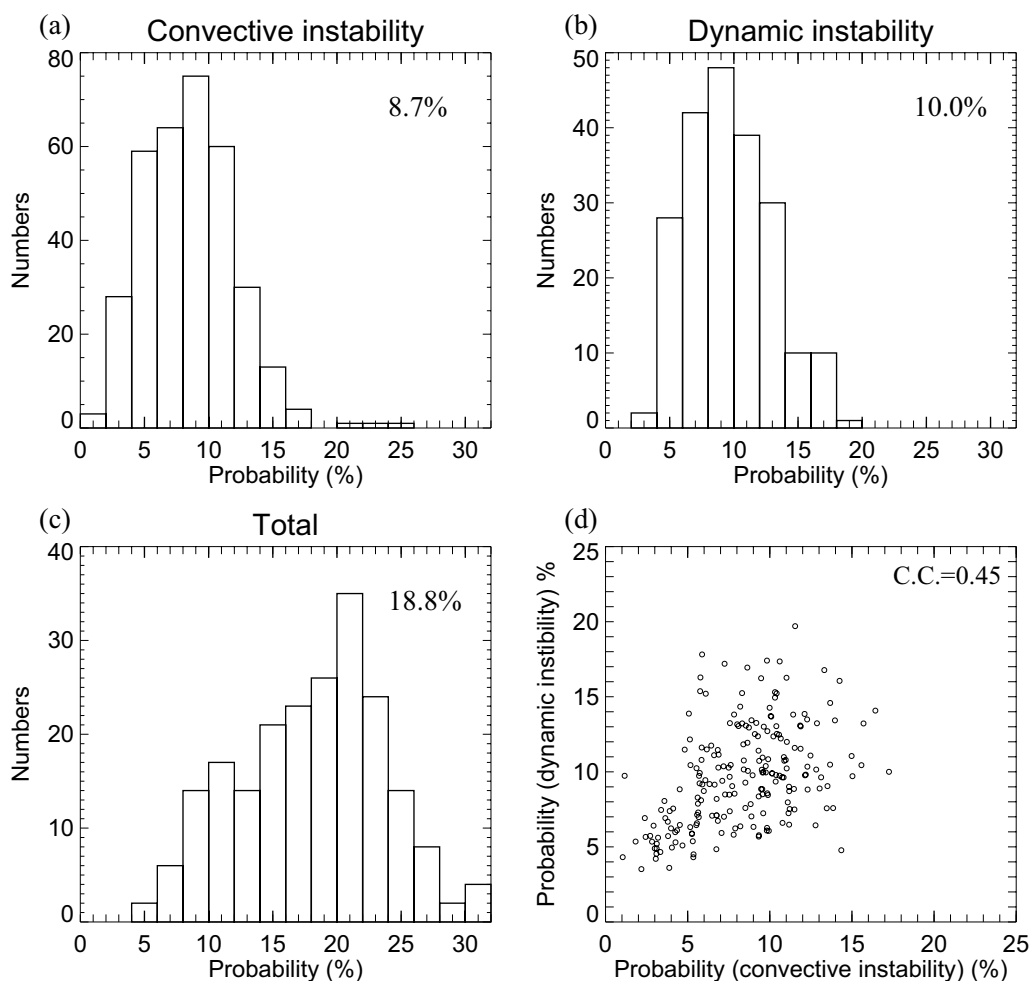


Fig. 4 Histograms of the number of days of the probabilities and correlations between the probabilities. Histograms of the number of days of the probabilities of the **a** convective and **b** dynamic instabilities, and **c** the total. **d** Scatter plots between the probabilities of the convective and dynamic instabilities. CC stands for correlation coefficient value

80 km (~22%), while it increases with height from 91 to 100 km (~9%). A similar but a slightly different shape is seen for an altitude profile of the probability of the dynamic instability; it varies with height less than that of the convective instability. The probability of the dynamic instability minimizes at 89 km with a value of ~8%, and is almost constant (below 10%) with height between 83 and 94 km. It increases above 94 km (except for 100 km) and below 83 km; it maximizes at 99 km (~15%) and it becomes ~12% at 80 km. The probability of the dynamic instability is larger (smaller) than that of the convective instability above (at and below) 86 km. The total probability (blue) shows a broad minimum with a value of ~12% between 89 and 92 km, and increases with height above (except for 100 km) and below. It becomes ~33% at 80 km and ~24% at 99 km. These results indicate

that the atmosphere around 89–92 km is the most stable between 80 and 100 km in the polar upper mesosphere in winter.

Discussion

We have presented the probabilities of the convective and dynamic instabilities between 80 and 100 km above Tromsø; they vary depending on the day as well as the altitude. Here, by considering the correlation with 3 kinds of parameters (12 h amplitude, F10.7 index, and local *K*-index), we discuss and suggest the causes of the convective and dynamic instabilities in the polar upper mesosphere.

Correlation with semidiurnal amplitudes

It is well known that the semidiurnal tide plays a dominant role in the dynamics in the upper mesosphere and

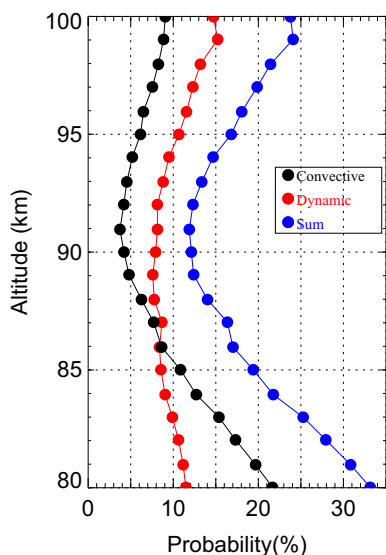


Fig. 5 Altitude profiles of the averaged probabilities of the convective and dynamic instabilities and the total. Altitude profiles of the averaged probabilities of the convective (black circles) and dynamic (red circles) instabilities and the total (blue circles) between 80 and 100 km

lower thermosphere at high latitudes (e.g., Pancheva et al. 2020; Nozawa et al. 2010), but its contribution to the convective and dynamic instabilities is not well understood. No such statistical study has been conducted. The semi-diurnal tide can directly contribute to establishing the background thermal structure, and also control the GW propagations and their dissipation. Beldon and Mitchell (2010) using MF radar data obtained at Rothera, Antarctica (68° S, 68° W) suggested that the critical level filtering imposed by tidal waves in the mesosphere occur when the tidal waves are westward phase in winter, and gravity wave activity increases when the tidal waves are eastward phase. Kinoshita et al. (2015) based on MF radar data obtained at Poker Flat (65° N, 147° W) showed that the GW kinetic energy exhibited two peaks reminiscent of semi-diurnal signatures in the altitude range of 78–90 km all over the year. Furthermore, they showed the phase of 12-h component of the GW kinetic energy followed the temporal variation of the phase of the 12-h component of the zonal wind. These studies indicate that the background atmosphere state is modulated by semi-diurnal tides and also has a tidal-phase dependency. In the present study, however, we only investigate the relation between atmospheric stability and semi-diurnal tidal amplitudes, and leave the phase dependency in future study.

We have derived 12-h periodic components (assuming the semi-diurnal tide), and here compare their amplitudes with the probabilities. The semi-diurnal tidal components

are derived for 248 nights (temperature data) and 154 nights (wind data). Those data have (longer than) 12-h data lengths with a data coverage larger than 55% at each height. Figure 6a, b, c examines possible correlations between the probabilities of the convective instability and averaged semi-diurnal amplitudes in northward and eastward wind (139 nights), and temperature (94 nights) data, respectively. The averaged semi-diurnal amplitudes are presented in Fig. 6 when semi-diurnal components are successfully derived (above 99% significance level) at more than 11 heights (out of 21 heights between 80 and 100 km) on any particular night. Owing to this criterion, the number of data is reduced. Correlation coefficients are 0.15 and 0.19 between the probabilities of the convective instability and the averaged amplitudes in northward and eastward wind data, respectively, indicating no correlations exist between them. From Fig. 6c, we can see a correlation (C.C. = 0.46) between the probabilities of the convective instability and the averaged semi-diurnal amplitudes in temperature data, implying that the semi-diurnal tide contributes to the convective instability, and other disturbances (probably GWs) are also involved. Figure 6d, e, f compares the probabilities of the dynamic instability with the averaged semi-diurnal amplitudes in the northward and eastward wind (139 nights), and temperature (67 nights) data, respectively. Correlation coefficients between the probabilities of the dynamic instability and northward and eastward winds are 0.52, while that between the probabilities of the dynamic instability and that of temperature is 0.36. Thus, a fairly good correlation is found between the probability of the dynamic instability and the semi-diurnal amplitudes of the winds.

When a different higher criterion is used in which data are available at more than 16 heights, the correlation coefficient becomes higher (although the number of nights is reduced). The correlation coefficients between the probabilities of the convective instability and the averaged amplitudes of the northward wind and temperature are 0.25 (102 nights) and 0.73 (25 nights), respectively, and the correlation coefficients between the probabilities of the dynamic instability and the averaged amplitudes of the northward and eastward winds, and temperature are 0.58 and 0.55 (102 nights), and 0.51 (20 nights). These results indicate that the semi-diurnal tide with large amplitudes plays an important role in causing the dynamic instability between 80 and 100 km in the polar MLT region, while it is an important but not dominant source for the convective instability.

Correlation with F10.7 flux

The F10.7 index is a good proxy for the Extreme Ultra Violet (EUV) flux, which partly ionizes the atmosphere in the

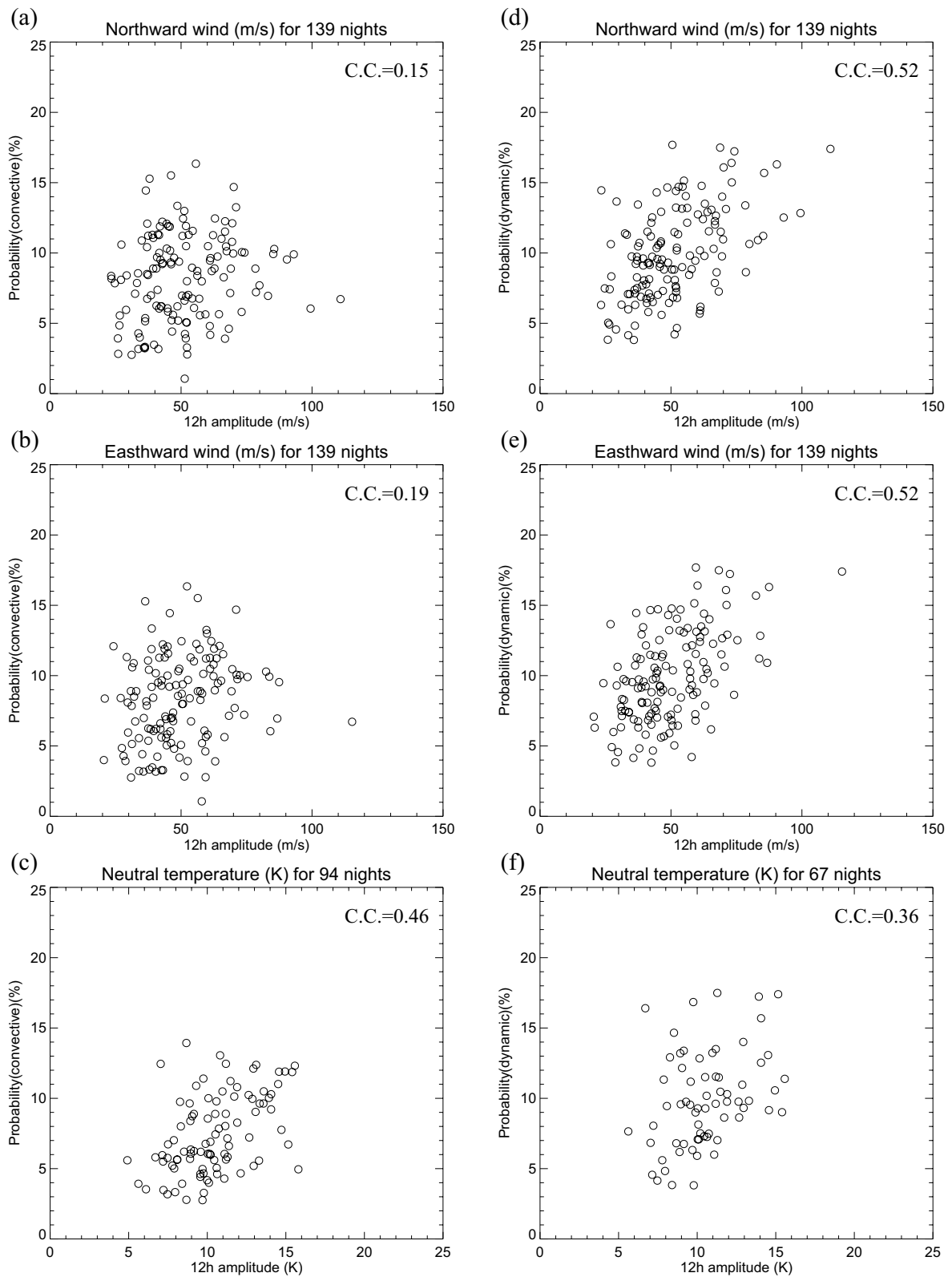


Fig. 6 Scatter plots between the semidiurnal tidal amplitudes and the probabilities of the convective and dynamic instabilities. Scatter plots between the averaged semidiurnal tidal amplitudes in **a** northward and **b** eastward winds, and **c** temperature data and the probability of the convective instability. Scatter plots between the averaged semidiurnal tidal amplitudes in **d** northward and **e** eastward winds, and **f** temperature data and the probability of the dynamic instability

mesosphere and thermosphere. It is expressed in the solar flux unit (sfu), where $1 \text{ sfu} = 10^{-22} \text{ W m}^{-2} \text{ Hz}^{-1}$ (Tapping 2013). Figure 7a, b shows temporal variations of the probabilities of the convective instability (338 nights; red circles) and the dynamic instability (210 nights; blue circles), respectively, as a function of time from October 2010 and 2012 to December 2019 together with the F10.7 flux (right scale). The F10.7 flux datum is not available on January 1, 2012. The F10.7 flux shows a well-known 11-year variation from ~ 70 to over 200 (sfu). The F10.7 flux was below 80 (sfu) in 2010 and from 2017 to 2019, while it was higher from 2011 to 2015 and sometimes exceeded 200 (sfu). The probabilities of the convective instability show day-to-day variations which would be due to those of tides and GWs. No trend can be found over the 9 years in terms of the solar cycle variation in Fig. 7a. This is confirmed by Fig. 7c showing a scatter plot between the F10.7 index and the probabilities of the convective instability with a correlation coefficient of 0.18. In Fig. 7b, day-to-day variations of the probability of the dynamic instability can be seen, and the probability tends to be higher as the F10.7 index is higher. This trend is clearly found in Fig. 7d which is a scatter plot between the F10.7 index and the probabilities of the dynamic instability. Its correlation coefficient is high (0.54). Thus, it can be said that the dynamic instability has dependence on the solar activity, while the convective instability does not. While this relationship is surprising, the causative mechanism is unclear, and we plan to investigate it separately in the future. This is beyond the scope of this paper.

Auroral effect

Tromsø is located under the auroral zone, so auroral effects would influence the atmospheric stability even in the upper mesosphere. Several studies have investigated the auroral effects on the lower thermosphere, and the wind system there has been reported to show some changes due to the geomagnetic disturbances at and above 105–107 km (e.g., Nozawa and Brekke 1995; Richmond et al. 2003). As far as we know, no studies have investigated the auroral effects on the occurrence of the atmospheric instabilities in the polar upper mesosphere. We assume no auroral effects on the lidar observations, since no strong auroral emissions exist around 589 nm. Figure 8a shows a scatter plot between probabilities of the convective instability and the local K -index (3 h resolution) for 339 nights. The

correlation coefficient is 0.22, implying there might be a (weak) correlation. Thus, here we have divided data into 3 height regions and calculated the probabilities at the individual height regions, such as between 94 and 100 km, 87 and 93 km, and 80 and 86 km; the results are, respectively, shown in Fig. 8b, c, d. Figure 8b shows a correlation (C.C.=0.45) between the local K -index and the probability of the convective instability between 94 and 100 km, while no good correlations are found at and below 93 km as shown in Fig. 8c, d. There appears to be a plasma–neutral coupling process, which influences the neutral thermal structure, between 94 and 100 km. The height region due to the particle heating by auroral electrons depends on their energy (e.g., Miyoshi et al. 2015; Turunen et al. 2009, and reference therein). The energetic electrons with energy between ~ 10 keV and ~ 20 keV can heat the atmosphere between ~ 90 and 100 km, and thus it would be possible to enhance the negative temperature gradient (and induce the generation of the convective instability) above the heating region. In addition, some chemical processes related to the sodium ionization would change the vertical thermal structure.

Figure 9a shows a scatter plot between the local K -index and the probabilities of the dynamic instabilities for 210 nights. No profound correlation can be found. This is the same with divided data in the three height regions shown in Fig. 9b–d. This is consistent with the previous studies about the auroral effect on the wind system found only at and above 105 km, suggesting auroral effects cannot reach below 105 km in the wind system. To summarize possible auroral effects on the instabilities, a fairly good correlation between the local K -index and the probability of the convective instability between 94 and 100 km was found, suggesting an auroral effect would influence the thermal structure even below 100 km.

Dependence on gravity wave dissipation

In Fig. 5, we showed an altitude profile of the probabilities of the convective instability, and the averaged probability decreases with increasing height between 80 and 91 km. Figure 10a, b, c shows altitude profiles of the averaged potential energy, Brunt–Väisälä frequency and period, respectively, between 80 and 100 km. To derive these values, we used 108 nights of data which have longer data lengths (longer than 16 h with a data coverage being larger than 0.55 at each height). The mean Brunt–Väisälä

(See figure on next page.)

Fig. 7 Temporal variations of F10.7 flux, probabilities of the convective and dynamic instabilities, and scatter plots between F10.7 flux and the probabilities. **a** Temporal variations of F10.7 flux (solid line) with the probability of the convective instability (red circles) from October 2010 to December 2019. **b** Temporal variations of F10.7 flux (solid line) with the probability of the dynamic instability (blue circles) from October 2012 to December 2019. **c** Scatter plots between F10.7 flux and the probability of the convective instability. **d** Scatter plots between F10.7 flux and the probability of the dynamic instability

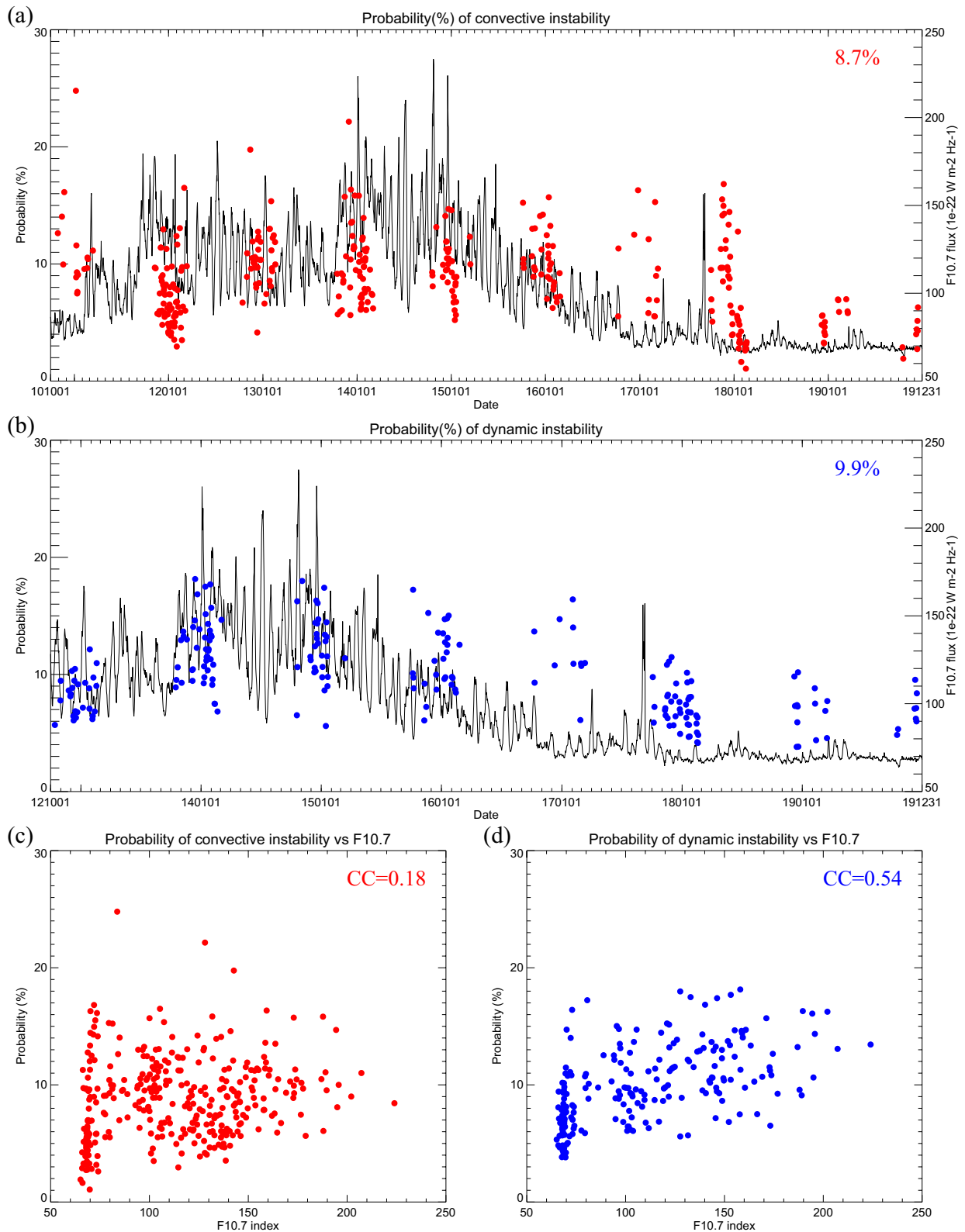


Fig. 7 (See legend on previous page.)

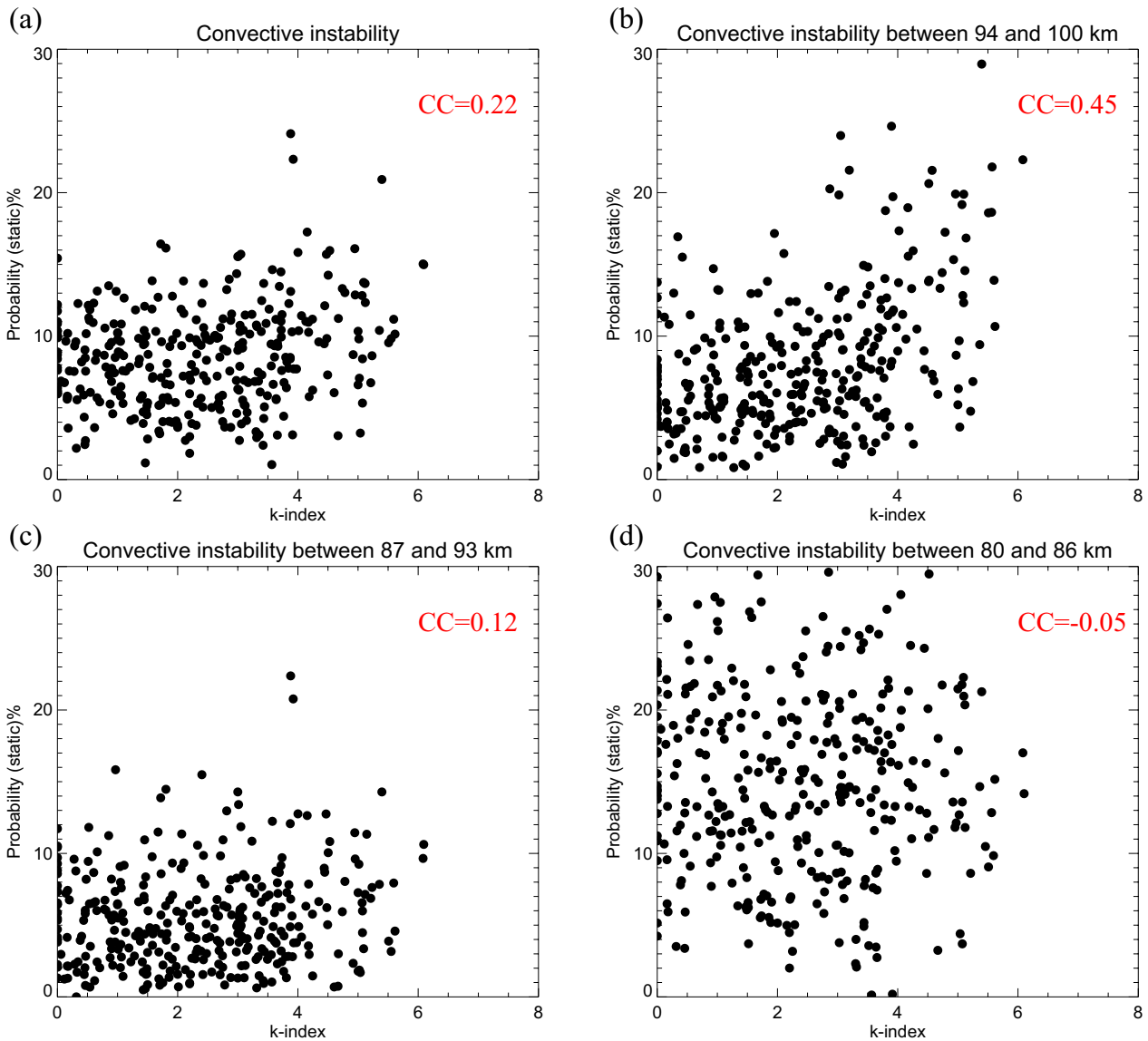


Fig. 8 Scatter plots between the *K*-index and the probability of the convective instability. Scatter plots between the *K*-index and the probability of the convective instability **a** between 80 and 100 km, **b** 94 and 100 km, **c** 87 and 93 km, and **d** 80 and 86 km

period is about 323 s (5.4 min) which is almost the same as those (~5.0 min) reported in Zhao et al. (2003) and Li et al. (2005) for middle latitudes.

Figure 10d shows the number of days averaged at each height. Between 86 and 94 km, the number of averaged data is 108 (days), and it decreases with decreasing height, and it is only 29 (days) at 80 km. The mean Brunt–Väisälä frequency ranges from 0.018 to 0.024 rad/s, and the mean Brunt–Väisälä period ranges from 263 to 349 s between 80 and 100 km as shown in Fig. 10b, c. The potential energy of gravity waves (GWs) as a function of height ($E_p(z)$) is defined as (e.g., Kogure et al. 2017; Kaifler et al. 2015):

$$E_p(z) = \frac{1}{2} \left(\frac{g}{N(z)} \right)^2 \overline{\left(\frac{T'(z, t)^2}{T_0(z, t)^2} \right)}. \quad (5)$$

To extract the background temperature $T_0(z, t)$ from the observed temperature $T(z, t)$, we employ a similar method described by Kaifler et al. (2015). Since in the upper mesosphere, amplitudes of tidal components are significantly large compared to GW perturbations, first we subtract 12-h, 8-h, and 6-h periodic components (so-called tidal components) from $T(z, t)$ at each height. The derived data are defined as $T_2(z, t)$. Next, a

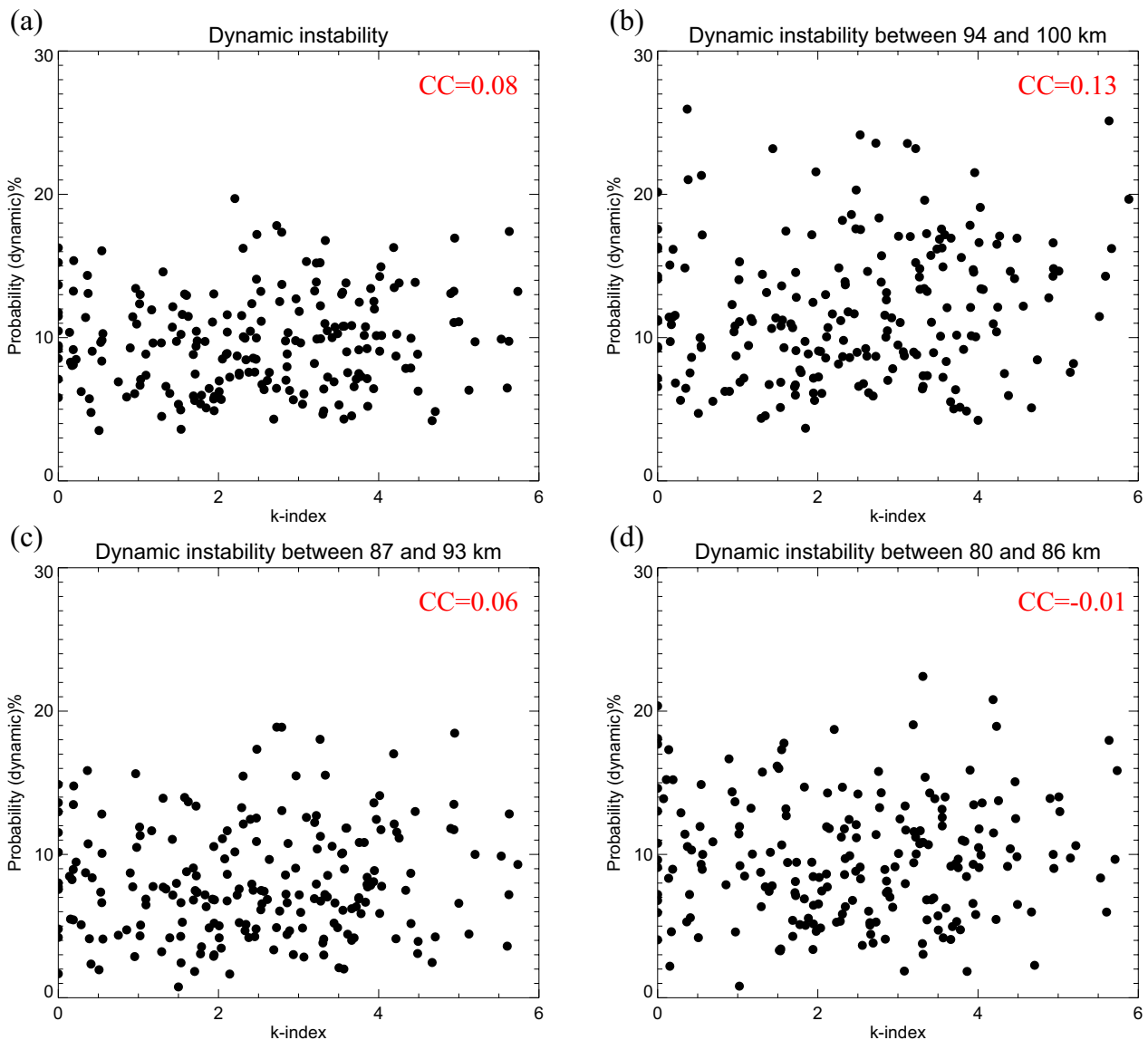


Fig. 9 Scatter plots between the *K*-index and the probability of the dynamic instability **a** between 80 and 100 km, **b** 94 and 100 km, **c** 87 and 93 km, and **d** 80 and 86 km

third-order polynomial is fitted to each altitude profile of $T_2(z, t)$, and then $T_0(z, t)$ is calculated at time t . Then, $T'(z, t)$ is derived by the following formula:

$$T'(z, t) = T_2(z, t) - T_0(z, t). \tag{6}$$

$T(z, t)$ is the observed (temperature) data at height z and time t . After deriving potential energy profiles for 108 nights, we averaged all of them as a function of altitude, and produced the averaged potential energy profile shown in Fig. 10a. The averaged potential energy is about ~ 121 J/kg at 82 km, and it generally decreases with increasing height between 82 and 89 km, and it becomes

about 64% of the value (~ 77 J/kg) at 89 km, indicating GW dissipation in the height region. Above 89 km, it generally increases with higher altitudes, but it is smaller than that without dissipation indicated by a thicker blue curve starting at 90 km ($=E_p(90 \text{ km}) \exp((z-90)/H)$) with a scale height H being 6 km assumed), suggesting that some GW dissipation occurs in this height region as well. The probability of the convective instability was also higher below 86 km, as shown in Fig. 5. The averaged potential energy of gravity waves shows decrease (less sharply) with height between 81 and 89 km, suggesting that dissipation of gravity waves plays an important role

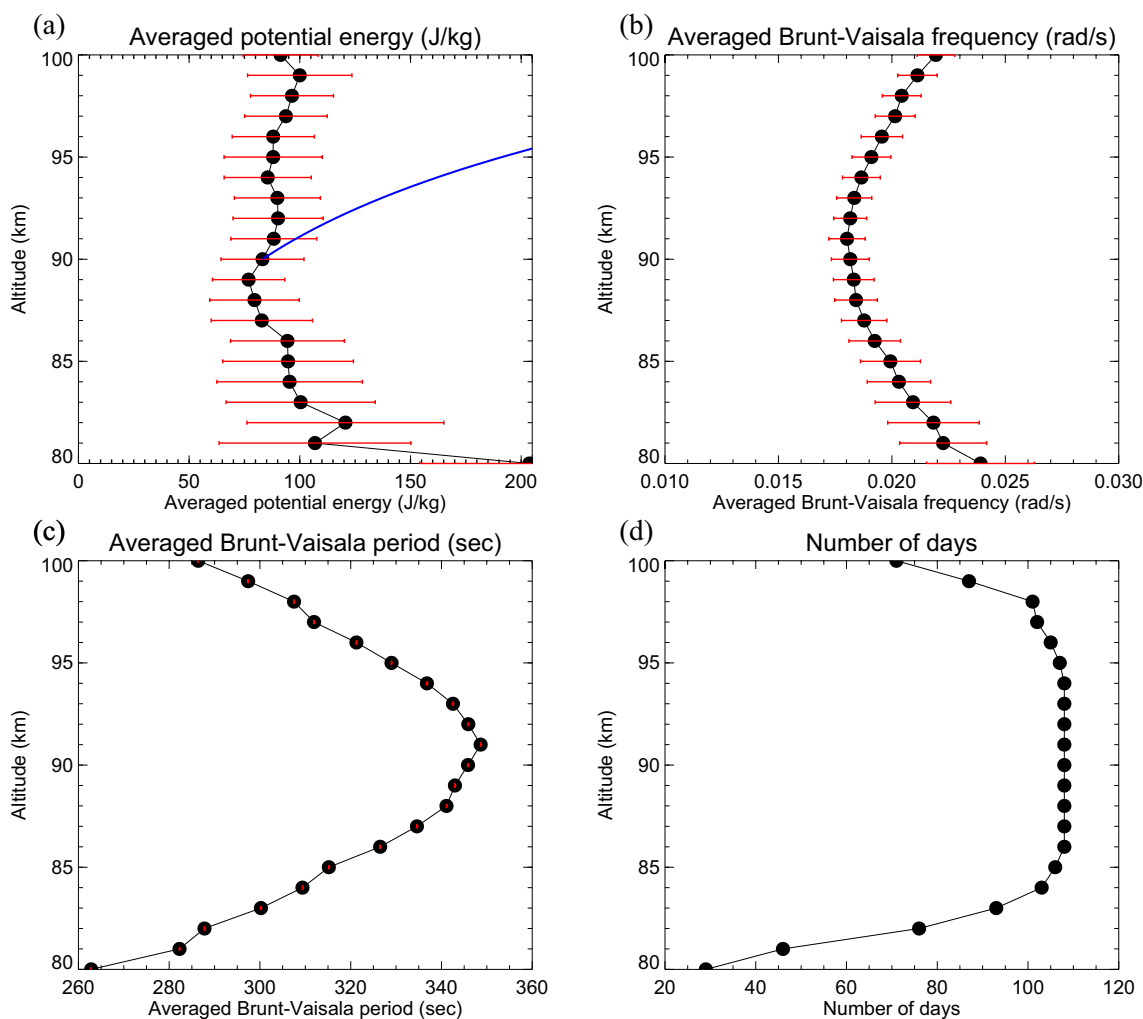


Fig. 10 Altitude profiles of averaged potential energy of GWs, Brunt–Väisälä frequency and period, and number of days used. Altitude profiles of **a** averaged potential energy of GWs together with a profile with no dissipation occurring (blue curve), **b** Brunt–Väisälä frequency, **c** Brunt–Väisälä period, and **d** number of days used. Horizontal bars in **a** and **b** denote a standard deviation

(at least partly) in causing the convective instability below 89 km. Since the negative slope of the GW potential energy is not sharp, GWs alone do not appear to explain the altitude profile of the convective instability occurrence, which is obviously influenced by the structure of N^2 and also the tidal amplitudes (12 h, and probably 8 h and 6 h). We would like to point out that the correlation coefficients for temperature amplitudes of the semidiurnal tide are much larger than those for wind amplitudes shown in Fig. 6a–c.

Comparison with other sites

We here compare our results (including data with other time/height resolutions) with those obtained at four low/middle latitude stations, such as Albuquerque, New Mexico (35.0° N, 106.5° W) by Zhao et al. (2003), Maui, Hawaii (20.7° N, 156.3° W) by Li et al. (2005), Fort Collins,

Colorado (41.1° N, 105.1° W) by Sherman and She (2006), and São José dos Campos (23.1° S, 45.9° W) by Andrioli et al. (2017). It should be kept in mind that data are compared with partly different time and height resolutions taken under different conditions (season, and solar activity). Table 1 compares the probabilities at Tromsø with those at the other sites. In Table 1, the probabilities with standard deviations at Tromsø with four sets of temporal and altitude resolutions are listed for comparison. The probabilities of the convective instability at Tromsø are 8.7% (6 min/1 km; SD=3.6%), 5.2% (15 min/1 km; SD=3.1%), 1.3% (15 min/2 km; SD=1.4%), and 0.9% (30 min/2 km; SD=1.1%). In general, the lower the resolutions are used, the lower the probabilities are calculated: one of the reasons for this is that short-period gravity wave perturbations that could induce the

Table 1 Comparison of probabilities of the convective and dynamic instabilities

Location	Tromsø (69.6° N, 19.2° E)	Albuquerque ^a (35° N, 106.5° W)	Maui ^b (20.7° N, 156.3° W)	Fort Collins ^c (41° N, 105° W)	SJDC ^d (23.1° S, 45.9° W)
Height range	80–100 km	80–105 km	85–100 km	80–105 km	82–98 km
Season	Winter	All seasons	All seasons	All seasons	All seasons ^e
Solar cycle	Full	Middle	High	High	Low
Data	339 nights 3725 h	32 nights 195 h	19 nights 133 h	63 nights 390 h	79 nights 589 h
Resolutions	(a) 6 min/1 km (b) 15 min/1 km (c) 15 min/2 km (d) 30 min/2 km	1.5 min/0.5 km	15 min/1 km	15 min/2 km	3 min/0.3 km
Probability of convective instability	(a) 8.7% (3.6%) (b) 5.2% (3.1%) (c) 1.3% (1.4%) (d) 0.9% (1.1%)	8.0%	2.9%	0.9% (1.4% in winter)	3.1%
Data	210 nights 2059 h	32 nights 195 h	19 nights 133 h	63 nights 390 h	79 nights 589 h
Resolutions	Same above	24 min/1 km	Same above	Same above	30 min/2 km
Probability dynamic instability	(a) 10.0% (3.5%) (b) 7.2% (3.1%) (c) 1.4% (1.3%) (d) 0.9% (1.1%)	7.5%	10.5%	4.4% (5.9% in winter)	17.5%

^a Zhao et al. (2003)

^b Li et al. (2005)

^c Sherman and She (2006)

^d Andrioli et al. (2017), SJDC stands for São José dos Campos

^e No summer data. A standard deviation is shown in parenthesis for Tromsø data

convective instability are smoothed out (Sherman and She 2006).

The probability of the convective instability at Tromsø appears to be higher than those at the other 4 sites. The temporal and height resolutions at Albuquerque and São José dos Campos are higher than those of Tromsø: these higher resolutions could not be achieved at Tromsø. The probabilities of the convective instability at Albuquerque (8.0%) and São José dos Campos (3.1%) are lower than that at Tromsø, even though the resolutions at the 2 sites are higher. For comparison with the 2 other sites, we have provided data with the same height and temporal resolutions, and compared the probabilities: the probability of the convective instability at Tromsø is higher than that at Maui (2.9%) and Fort Collins (0.9%). The probability at Fort Collins in winter is almost the same to that in Tromsø. The reasons the probability of the convective instability at Tromsø is higher than those at the other 3 sites (except for Fort Collins) are not yet clear at this point. One possible reason is a latitude difference, and there could be an auroral effect as shown in Fig. 8b. To clarify the auroral effect, we need simultaneous observations with auroral cameras, a photometer, and the Incoherent Scatter (IS) radar (i.e., EISCAT radar) which can observe auroral

effects more accurately in the ionosphere, and also derive the neutral wind and temperature in the lower Thermosphere (cf. Nozawa et al. 2006). Another possible reason is a seasonal effect: almost all of our data were obtained in winter (in particular in December and January) when it is the most convective unstable (Zhao et al. 2003; Sherman and She 2006).

The probability of the dynamic stability with 15 min/1 km resolutions at Tromsø (7.2%; SD=3.1%) is similar to that at Maui (10.5%) and at Albuquerque (7.5%), though the time resolution at Albuquerque is longer than that at Tromsø. The probability of the dynamic instability with 15 min/2 km resolutions at Tromsø (1.4%; SD=1.3%) is smaller than that at Fort Collins (4.4%; 5.9% in winter). One possible reason is that Sherman and She (2006) included data between 100 and 105 km where the higher probability would be expected due to larger wind shear. Another possible reason is that Sherman and She (2006) used data obtained under high solar cycle conditions when the probability tends to be higher. Thus, we can conclude that the probabilities of the dynamic instability at Tromsø and the 3 sites are similar. On the other hand, the probability with 30 min/2 km resolutions at Tromsø (0.9%; SD=1.1%) (and at the 3

sites as well) is significantly smaller than that at São José dos Campos (17.5%).

The shapes of altitude profiles of the probabilities of the convective and dynamic instabilities at Tromsø (shown in Fig. 5) are similar to those at Maui by Li et al. (2005). In particular, the sharp decrease of the probabilities of the convective instability from 85 to 89 km with height increasing is similar to that of our results. Also, the altitude profile of the probability of the dynamical instability where the authors pointed out the dynamical instability occurring in the upper mesopause region (93–100 km) more than in the lower region (85–93 km) is similar to our result shown in Fig. 5, although our results show the higher probability of the dynamical instability below 85 km which they did not observe. To summarize the comparisons, in general the probability of the convective instability at Tromsø is higher than those at middle/low latitudes, while the probability of the dynamic instability is similar to those except for São José dos Campos where an unusual large value is shown.

What causes the convective and dynamic instabilities?

The probability of the convective instability has dependence on the local K -index between 94 and 100 km, slight dependence on the semidiurnal amplitude (temperature data), and no dependence on the F10.7 flux. GWs show dissipation over the height region, and larger dissipation between 81 and 89 km where the probability of the convective instability is higher. The probability of the convective instability at Tromsø is higher than those at the 3 other sites except for Fort Collins. Thus, at Tromsø, the semidiurnal tide and GWs (in particular, those below 87 km) play an important role in the convective instability, and additionally an auroral effect would work between 94 and 100 km.

On the other hand, the probability of the dynamic instability has clear dependences on the semidiurnal amplitude (wind) and the F10.7 flux, and no dependence on the local K -index. Thus for the dynamic instability, the semidiurnal tide plays an important role together with GWs, but no auroral effect is detected. An unknown mechanism due to EUV also appears to play a role. An investigation of the mechanism is left for a future study.

Summary

We have presented the probabilities of the convective and dynamic instabilities between 80 and 100 km above Tromsø (69.6° N, 19.2° E) utilizing temperature and wind data obtained by the sodium lidar at Tromsø. This is the first statistical study on the convective and dynamic instabilities at high latitudes. Observations were made mainly in polar winter in November, December, January, and February. Only data having 4 h (at shortest)

data length with 5 K (at largest) temperature error and 15 m/s (at largest) wind velocity error are used. Using the square of the Brunt–Väisälä frequency (N^2) for 339 nights (3725 h) obtained from October 2010 to December 2019, and the Richardson number (Ri) for 210 nights (2059 h) obtained between October 2012 to December 2019, we calculated probabilities of the convective instability ($N^2 < 0$) and the dynamic instability ($0 \leq \text{Ri} < 0.25$). When we used data with 6 min/1 km resolutions, the probability of the convective instability varied from about 1% to 24% with a mean value of 8.7%, while that of the dynamic instability varied from 4 to 20% with a mean value of 10%. Both the probabilities showed no clear monthly variations from October to March, but large day-to-day variabilities are found.

We compared the probabilities with the F10.7 index and the local K -index to investigate solar cycle dependence and auroral disturbance dependence, respectively. The probability of the convective instability does not show a clear solar cycle dependence (F10.7 index), while it showed a dependence of geomagnetic activity (local K -index) (its correlation coefficient being 0.45) between 94 and 100 km. This would suggest an auroral influence on the atmospheric stability in the polar upper mesosphere. On the other hand, the probability of the dynamic instability showed a solar cycle dependence (its correlation coefficient being 0.54), while it did not show dependence of the geomagnetic activity.

We derived 12-h periodic components (assuming the semidiurnal tide in this study) for 248 nights (temperature) and 154 nights (wind), and compared them with the probabilities to evaluate contributions of the semidiurnal tide to the stabilities. The probability of the convective instability shows a dependence of the semidiurnal amplitude in temperature (C.C. = 0.46), and the probability of the dynamic instability shows dependence of the semidiurnal amplitude (C.C. = 0.52 for the northward and eastward winds). The averaged potential energy of GWs shows decrease with height at and below 89 km, suggesting that dissipation of GWs plays an important role in causing the convective instability at and below 89 km.

New major findings in this paper can be summarized as follows: (1) the probability of the convective instability between 94 and 100 km shows dependence on the local K -index (possibly an auroral effect). (2) The probability of the dynamic instability shows clear dependence on F10.7 index as well as semidiurnal tide (wind data). (3) The probability of the convective instability at Tromsø (located at high latitudes) is higher than those at middle/low latitudes except for Fort Collins. (4) The probability of the dynamic instability at Tromsø is similar to those at middle/low latitudes except for that at São José dos Campos.

Based on these observational results, we have concluded that (1) for the convective instability, the semidiurnal tide, GWs (in particular, those at and below 89 km), and an auroral effect (between 94 and 100 km) play important roles, and (2) for the dynamic instability, the semidiurnal tide plays an important role, and GWs and an unknown mechanism due to EUV also appear to play important roles. Investigation of the mechanisms of the auroral effect and due to EUV is left for future studies.

Abbreviations

C.C.	Correlation coefficient
EISCAT	European Incoherent Scatter
EUV	Extreme ultraviolet
GW	Gravity wave
Lidar	Light detection and ranging
MLT	Mesosphere and lower thermosphere
SD	Standard deviation
Sq	Solar Quiet

Acknowledgements

S.N. thanks Dr. K. Hocke for letting to use his Lomb-Scargle periodogram method routines. The local K-index is provided by TGO, UiT The Arctic University of Tromsø. We thank the EISCAT staff for supporting the lidar observations.

Author contributions

SN: led the study, made observations and data analysis, and provided and discussed scientific results. NS: contributed to development and maintenance of the lidar system and made observations. TK, SW: contributed to development and maintenance of the lidar system. TTT: contributed to development and maintenance of the lidar system, made observations, and discussed scientific results. SM: made data analysis and discussed scientific results. TT, HF: contributed to maintaining the lidar system, made observations, and discussed scientific results. LNV: discussed scientific results. MGJ: contributed to maintaining the lidar system, and provided the local K-index data. All authors read and approved the final manuscript.

Funding

This research has been partly supported by a Grant-in-Aid for Scientific Research A (21H04516, 21H04518) and B (17H02968, 19H01952, 21H01142, 21H01144), and a Grant-in-Aid for Exploratory Research (20K20940). This work is partially supported by Nagoya University Research Fund. VL Narayanan is supported by the Natural Environment Research Council (NERC), UK (grant no. NE/V01837X/1).

Availability of data and materials

All data generated or analyzed during this study are available at <https://www.isee.nagoya-u.ac.jp/~nozawa/indexlidardata.html>; <https://spaceweather.gc.ca/solarflux/sx-5-en.php>; <https://flux.phys.uit.no/Kindice/>.

Declarations

Ethics approval and consent to participate

Not applicable.

Consent for publication

Not applicable.

Competing interests

The authors declare no competing interests.

Author details

¹Institute for Space-Earth Environmental Research, Nagoya University, Nagoya, Japan. ²RIKEN Center for Advanced Photonics, RIKEN, Wako, Japan. ³Faculty of Engineering, Shinshu University, Nagano, Japan. ⁴Department of Computer and Network Engineering, University of Electro-Communications, Chofu,

Japan. ⁵Electronic Navigation Research Institute, National Institute of Maritime, Port and Aviation Technology, Mitaka, Japan. ⁶Faculty of Science and Technology, Seikei University, Musashino, Japan. ⁷Department of Electronic and Electrical Engineering, University of Bath, United Kingdom. ⁸Tromsø Geophysical Observatory, UiT The Arctic University of Norway, Tromsø, Norway.

Received: 16 June 2022 Accepted: 14 January 2023

Published online: 15 February 2023

References

- Andrioli VF, Batista PP, Xu J, Yang G, Chi W, Zhengkuan L (2017) Strong temperature gradients and vertical wind shear on MLT region associated to instability source at 23°S. *J Geophys Res Space Phys* 122:4500–4511
- Bartels J, Heck NH, Johnston HF, The three-hour-range index measuring geomagnetic activity (1939) Terrestrial magnetism and atmospheric electricity. *J Geophys Res* 44:411. <https://doi.org/10.1029/TE044i004p00411>
- Beldon CL, Mitchell NJ (2010) Gravity wave-tidal interactions in the mesosphere and lower thermosphere over Rothera, Antarctica (68°S, 68°W). *J Geophys Res* 115:D18101. <https://doi.org/10.1029/2009JD013617>
- Emanuel KA (1994) Atmospheric convection. Oxford University Press, New York, p 580
- Fritts DC, Alexander MJ (2003) Gravity wave dynamics and effects in the middle atmosphere. *Rev Geophys*. <https://doi.org/10.1029/2001RG000106>
- Hocke K (1998) Phase estimation with the Lomb-Scargle periodogram method. *Ann Geophys* 16:356–358
- Kaifler B, Lübken F-J, Höffner J, Morris RJ, Viehl TP (2015) Lidar observations of gravity wave activity in the middle atmosphere over Davis (69°S, 78°E), Antarctica. *J Geophys Res Atmos* 120:4506–4521. <https://doi.org/10.1002/2014JD022879>
- Kawahara TD, Nozawa S, Saito N, Kawabata T, Tsuda TT, Wada S (2017) Sodium temperature/wind LIDAR based on laser-diode-pumped Nd:Yag lasers deployed at Tromsø, Norway (69.6°, 19.2°). *Opt Express* 25:A491–A501
- Kinoshita T, Murayama Y, Kawamura S (2015) Tidal modulations of mesospheric gravity wave kinetic energy observed with MF radar at Poker Flat Research Range, Alaska. *J Geophys Res Atmos* 120:6379–6390. <https://doi.org/10.1002/2014JD022647>
- Kogure M, Nakamura T, Ejiri MK, Nishiyama T, Tomikawa Y, Tsutsumi M, Suzuki H, Tsuda TT, Kawahara TD, Abo M (2017) Rayleigh/Raman lidar observations of gravity wave activity from 15 to 70 km altitude over Syowa (69°S, 40°E), the Antarctic. *J Geophys Res Atmos* 122:7869–7880
- Kundu PK, Cohen IM, Dowling DR (1990) Fluid mechanics. Academic Press, San Diego, p 638
- Li F, Liu AZ, Swenson GR (2005) Characteristics of instabilities in the mesopause region over Maui, Hawaii. *J Geophys Res* 110:D09S12
- Miyoshi Y, Oyama S, Saito S, Kurita S, Fujiwara H, Kataoka R, Ebihara Y, Kletzing C, Reeves G, Santolik O, Clilverd M, Rodger CJ, Turunen E, Tsuchiya F (2015) Energetic electron precipitation associated with pulsating aurora: EISCAT and Van Allen Probe observations. *J Geophys Res Space Phys* 120:2754–2766. <https://doi.org/10.1002/2014JA020690>
- Nozawa S, Brekke A (1995) Studies of the E region neutral wind in the disturbed auroral ionosphere. *J Geophys Res* 100:14717–14734
- Nozawa S, Ogawa Y, Brekke A, Tsuda T, Hall CM, Miyaoka H, Kurihara J, Abe T, Fujii R (2006) EISCAT observational results during the DELTA campaign. *Earth Planets Sci* 58:1183–1192
- Nozawa S, Ogawa Y, Oyama S, Fujiwara H, Tsuda T, Brekke A, Hall C, Murayama Y, Kawamura S, Miyaoka H, Fujii R (2010) Tidal waves in the polar lower thermosphere using the EISCAT long run data set obtained in September 2005. *J Geophys Res* 115:A08312. <https://doi.org/10.1029/2009JA015237>
- Nozawa S, Kawahara TD, Saito N, Hall CM, Tsuda TT, Kawabata T, Wada S, Brekke A, Takahashi T, Fujiwara H, Ogawa Y, Fujii R (2014) Variations of the neutral temperature and sodium density between 80 and 107 km above Tromsø during the winter of 2010–2011 by a new solid state sodium LIDAR. *J Geophys Res* 119:441–451. <https://doi.org/10.1002/2013JA019520>
- Nozawa S, Kawabata T, Hosokawa K, Ogawa Y, Tsuda T, Mizuno A, Fujii R, Hall C (2018) A new five-wavelength photometer operated in Tromsø (69.6°N, 19.2°E). *Earth Planets Space* 70:193. <https://doi.org/10.1186/s40623-018-0962-x>

- Pancheva D, Mukhtarov P, Hall C, Meek C, Tsutsumi M, Pedatella N, Nozawa S, Manson A (2020) Climatology of the main (24-h and 12-h) tides observed by meteor radars at Svalbard and Tromsø: comparison with the models CMAM-DAS and WACCM-X. *JASTP* 207:105339. <https://doi.org/10.1016/j.jastp.2020.105339>
- Richmond AD, Lathuillière C, Vennerstroem S (2003) Winds in the high-latitude lower thermosphere: dependence on the interplanetary magnetic field. *Geophys Res*. <https://doi.org/10.1029/2002JA009493>
- Sedlak R, Hannawald P, Schmidt C, Wüst S, Bittner M, Stanic S (2021) Gravity wave instability structures and turbulence from more than 1.5 years of OH⁺ airglow imager observations in Slovenia. *Atmos Meas Tech* 14:6821–6833
- She CY, Yu JR (1994) Simultaneous three-frequency Na lidar measurements of radial wind and temperature in the mesopause region. *Geophys Res Lett* 21:1771–1774
- Sherman JP, She CY (2006) Seasonal variation of mesopause region wind shears, convective and dynamic instabilities above Fort Collins, CO: a statistical study. *J Atmos Sol Terr Phys* 68:1061–1074
- Stull R (2020) Practical meteorology, LibreTexts GEOSCIENCE. [https://geo.libretexts.org/Bookshelves/Meteorology_and_Climate_Science/Book%3A_Practical_Meteorology_\(Stull\)/05%3A_Atmospheric_Stability/5.08%3A_Flow_Stability](https://geo.libretexts.org/Bookshelves/Meteorology_and_Climate_Science/Book%3A_Practical_Meteorology_(Stull)/05%3A_Atmospheric_Stability/5.08%3A_Flow_Stability)
- Tapping KF (2013) The 10.7 cm solar radio flux ($F_{10.7}$). *Space Weather* 11:394–406. <https://doi.org/10.1002/swe.20054>
- Turunen E, Verronen PT, Seppälä A, Rodger CJ, Clilverd MA, Tamminen J, Enell C-F, Ulich T (2009) Impact of different energies of precipitating particles on NO_x generation in the middle and upper atmosphere during geomagnetic storms. *J Atmos Sol Terr Phys* 71:1176–1189
- Zhao Y, Liu AZ, Gardner CS (2003) Measurements of atmospheric stability in the mesopause region at Starfire Optical Range, NM. *J Terr Sol Atmos Phys* 65:219–232

Publisher's Note

Springer Nature remains neutral with regard to jurisdictional claims in published maps and institutional affiliations.

Submit your manuscript to a SpringerOpen[®] journal and benefit from:

- Convenient online submission
- Rigorous peer review
- Open access: articles freely available online
- High visibility within the field
- Retaining the copyright to your article

Submit your next manuscript at ► [springeropen.com](https://www.springeropen.com)
